Hindawi
Advances in Meteorology
Volume 2022, Article ID 1611015, 19 pages
https://doi.org/10.1155/2022/1611015

Research Article

Temporal-Spatial Characteristics and Future Changes of Temperature Extremes in Longtan Watershed Based on Multiple Indices

Chongxun Mo,[1,2,3] Shiting Long,[1,2,3] Yuli Ruan,[1,2,3] Yanping Xie,[4] Xingbi Lei,[1,2,3] Shufeng Lai,[1,2,3] Guikai Sun,[1,2,3] and Zhenxiang Xing[5]

[1]*College of Architecture and Civil Engineering, Guangxi University, Nanning 530004, China*
[2]*Guangxi Provincial Engineering Research Center of Water Security and Intelligent Control for Karst Region, Guangxi University, Nanning 530004, China*
[3]*Key Laboratory of Disaster Prevention and Structural Safety of Ministry of Education, College of Civil Engineering and Architecture, Guangxi University, Nanning 530004, China*
[4]*Guangxi Datengxia Industrial Management Co. LTD, Nanning 530200, China*
[5]*School of Water Conservancy and Civil Engineering, Northeast Agricultural University, Haerbin 150000, China*

Correspondence should be addressed to Yuli Ruan; 1810401017@st.gxu.edu.cn

Received 30 December 2021; Revised 15 April 2022; Accepted 18 April 2022; Published 3 May 2022

Academic Editor: Nir Y. Krakauer

Global warming and the intensification of extreme temperature events have been major issues around the world in recent decades. Understanding changes in temperature extremes is critical to assessing and responding to the risks associated with regional temperature change. This paper takes the Longtan watershed as the research object, and 11 extreme temperature indices were calculated based on the meteorological observation data from 1959 to 2017. The Mann-Kendall trend mutation test, Empirical Orthogonal Function, and other methods were used to explore the spatial and temporal distribution characteristics of temperature extremes. Meanwhile, the simulation effects of temperature were analyzed based on 11 CMIP5 climate models, and the extreme temperature change in 2021–2050 under the high emission scenario RCP8.5 and low emission scenario RCP4.5 was estimated. The main results are as follows: both the warm-related indices and the extreme minimum temperature show an increasing trend. The cold-related frequency indices all show a decreasing trend. The spatial distribution of most temperature extremes increases or decreases from southwest to northeast, and the fluctuation is obvious with the alternation of positive and negative positions of the time. In the next 30 years, compared with the reference period 1961–1990, under the RCP4.5, the multiyear average of the Extreme T_{max} and the multiyear average of the Extreme T_{min} increase by 2.1°C and 0.4°C, respectively, and by 2.0°C and 0.3°C under the RCP8.5. Overall, the frequency of extreme cold events decreases, and the frequency of extreme warm events increases. There is a warming trend in temperature extremes.

1. Introduction

Since the 20th century, as the global climate continues to warm, the frequency of extreme temperature events has increased significantly, and a series of problems caused by climate change have aroused wide public concern. For example, the summer heat wave that occurred in Japan in 2007 reached a maximum temperature of 40.9°C [1]. An extreme cold surge event caused record-breaking low temperatures in East Asia during 20–25 January 2016 [2]. From the 1960s to the 2010s, the Diurnal temperature range (DTR) decreased significantly in China, the warm extremes increase significantly, and the hot extremes continue the significant warming trend nationally and in climate regions of East China, Southwest China, and the Tibetan Plateau [3–5]. Regarding Iturbide et al. [6] bias adjustment for predicted changes in extreme heat, the results unveil a stronger and more rapid increase of the frequency of heat extremes in the

future than that one may expect using the raw model outputs alone. Long-term changes to Earth's energy balance are increasing the frequency and intensity of many extreme events and the likelihood of compound events, with trends being projected to accelerate under certain greenhouse gas emissions scenarios [7]. The intensification of extreme temperature events has caused serious damage to ecological and socioeconomic environments. According to the Fifth Assessment Report of the International Intergovernmental Panel on Climate Change (IPCC), the global average temperature increased by 0.65–1.06°C from 1880 to 2012. As global warming increases, extreme temperature events will occur frequently in the future [8]. Therefore, it is important to analyze the historical spatial and temporal variability of temperature extremes and their future trends. Differences between climate models tend to make the results of climate predictions uncertain, and it is necessary to evaluate the simulation effects of different models [9]. Therefore, a suitable climate model for the study basin needs to be selected to provide the basis for future urban strategy development. The increase in extreme temperature events can have significant negative impacts on society, which include changes in ecosystems, disruption in food production and water supply, destruction of infrastructure and residential areas, and increased morbidity and mortality [10, 11]. Analysis of temperature extremes is important in terms of helping to carry out meteorological disaster prediction and early warning studies and reducing the negative impacts of extreme temperature events on local production and life.

In recent years, extreme temperature events have been extensively studied by many scholars from different perspectives. On a global scale, the cold days (TX10p) and cold nights (TN10p) had decreased, and the warm days (TX90p) and warm nights (TN90p) had increased across Indonesia over the past 30 years, showing a clear warming trend [12]. New Zealand [13], Nepal [14], Barbados, and Caribbean [15] all showed trends of increasing extreme high temperature events and decreasing extreme low temperature events. For China, the trends of extreme temperatures were consistent with global trends. Some scholars [16] have studied extreme temperatures in northwest China from 1960 to 2004 and concluded that the spatial distribution of extreme high and extreme low temperature events could be divided into five subregions, namely, northern Qinghai and western Gansu, northern Xinjiang, southern Xinjiang, eastern northwest China, and southern Qinghai; all of these five regions showed a significant increasing trend of extreme high temperature events. Extreme temperatures have regional and seasonal characteristics, with increasing trends in both autumn and winter, and decreasing trends in both spring and summer. The extreme low temperature events have a significant increasing trend in the northern basin of China, while the extreme high temperature events have an insignificant or even decreasing trend in the southern region of China [17]. Zhan et al. [18] analyzed the extreme temperature characteristics of global land regions based on coupled 37 climate model simulations of CMIP5, and the results showed that the probability of both dry/wet and hot/cold events will increase under both RCP4.5 and RCP8.5 emission scenarios.

Although many scholars have used different methods to study the characteristics of the spatial and temporal distribution of temperature extremes and future trends, there are still some urgent problems that need to be solved: (1) Most studies have used a single or inadequate index to analyze the spatial and temporal characteristics of temperature extremes, but comprehensive analysis of extreme temperatures is still relatively rare; (2) no single climate model has been accepted as a global standard, and how to select the best climate models still requires further study; and (3) there is still lack of long-tern temperature extremes trend analysis in Longtan watershed. Therefore, this study aims to comprehensively examine temporal-spatial characteristics and future trends of temperature extremes in the watershed. It can contribute to the response to climate change, and reduce the negative impacts of extreme temperature events on the ecological environment and people's production and life. The research framework mainly includes the following: (1) analyzing the spatial and temporal characteristics of extreme temperature changes; (2) selecting the climate models; (3) predicting the extreme temperature changes in the watershed from 2021 to 2050.

2. Study Area and Data

Longtan watershed is distributed at the junction of Yunnan, Guizhou, and Guangxi provinces with a geographical location of 102°14′E~107°32′E, 23°11′N~27°01′N. The watershed covers an area of 98500 km^2. The topography of the watershed gradually decreases from northwest to southeast. It is located in the southeast of the Yunnan-Guizhou Plateau and the area south of the Guizhou Plateau. The terrain is rugged and complex with plateaus, mountains, hills, and basins intermixed. The limestone is widely distributed, the landform is mainly an erosion landform, and karst development is extensive. The basin belongs to the subtropical climate zone, with high temperatures and rain in summer, and dry winters with little rain. The average annual temperature is 20.1°C, the extreme maximum temperature is 38.9°C, and the extreme minimum temperature is −2.9°C. The Longtan Water Control Project was prepared for construction in 1990s in the basin, with an installed capacity of 6.3 million kw and an annual power generation capacity of 18.7 billion kw·h. It is a landmark project of "west-east power transmission" and a key project of China's Western Development Policy.

In this study, historical observations of daily maximum and daily minimum temperatures from 15 meteorological stations within and adjacent to the Longtan watershed were obtained from the China Meteorological Data Center (https://data.cma.cn/wa). The daily missing data of meteorological stations for some years were interpolated by using the correlation of adjacent stations. The distribution of stations is shown in Figure 1. The temporal and spatial characteristics of extreme temperature were analyzed based on the 27 extreme climate indices proposed by the ETCCDI expert group [19]. Longtan watershed belongs to the

subtropical climate zone, and some indices show a little temporal trend, and some indices are continuously zero, such as the number of frost days, which is extremely rare in the watershed. According to the situation of the study area, 11 extreme temperature indices including both cold and warm extreme temperature were selected from a total of 27 extreme climate indices, which are shown in Table 1, including 3 intensity indices, 6 frequency indices, and 2 duration indices. All extreme temperature indices in this study were annualized using 1961–1990 as the base period. Model selection and analysis of future changes in extreme temperatures referring to the results of Chen et al. [20] and Xiao et al. [21] assessment of the simulation capability of CMIP5 climate models in the Chinese region, 11 CMIP5 climate models with a daily scale were selected, and the data under the high emission (RCP8.5) and low emission (RCP4.5) scenarios from 2021 to 2050 were applied to study in the Longtan Basin. The climate models are shown in Table 2, and the data of the climate models are obtained from the CMIP5 official website (https://esgf-node.llnl.gov/search/cmip5/). To compare those with the station data, downscaling methods are often used to process the model output data. Due to the limited information available, the inverse distance weighted (IDW) method [22] was adopted to downscale the grid data of the model information to the sites; that is, the four grid points of the grid were interpolated to the stations.

3. Methodology

The main research methods applied in this study can be divided into four parts. (1) The Kendall rank correlation method [23], Spearman rank correlation method [24], and linear trend regression method [25] were used for significance testing, and the trends of each extreme temperature index were analyzed by combining the three methods. The M-K trend mutation test was adopted to further analyze the variation characteristics of extreme temperature in different years, combined with the sliding t-test to analyze the mutation trend [26]. (2) The Empirical Orthogonal Function (EOF) method was applied to analyze the spatial characteristics of extreme temperature. The significance of the decomposed modes was tested using the North criterion. Then, the significant modes and their corresponding time coefficients were analyzed. The mode that passes the significance test maximally characterized the distribution structure of the variability of extreme temperature in the Longtan watershed. (3) The simulation effects of 11 climate models were evaluated by composite rating metrics to select a suitable climate model for the Longtan watershed. (4) Based on the selected climate model, the future extreme temperature changes in the basin under different emission scenarios were analyzed.

3.1. M-K Trend Mutation Test. Mann-Kendall trend mutation test is a widely used trend analysis method in the field of meteorology. The test series does not need to follow a certain distribution. The method is not disturbed by outliers and is easy to calculate [27–29]. For a sequence $x_1, x_2, \ldots, x_n$ of n sample sizes, construct the statistical variables:

$$S_k = \sum_{i=1}^{k} r_i \quad k = 2, 3, \ldots, n,$$
$$r_i = \begin{cases} 1, & x_j > x_i, \\ 0, & x_j \le x_i, \end{cases} \quad j = 1, 2, \ldots, i, \tag{1}$$

where S_k denotes the total number of ith sample $x_i > x_j\,(1 \le i \le j)$. Assuming that the S_k are randomly independent, their means and variances are calculated as follows:

$$E(S_k) = \frac{k(k-1)}{4},$$
$$\mathrm{Var}(S_k) = \frac{k(k-1)(2k+5)}{72}, \tag{2}$$
$$k = 1, 2, \ldots, n.$$

The standardized statistics for the one-tailed test are formulated as

$$UF_k = \frac{(S_k - E(S_k))}{\sqrt{\mathrm{Var}(S_k)}}, \tag{3}$$

where $UF_1 = 0$. When $UF_k > 0$, the sequence shows an upward trend; otherwise, it shows a downward trend. At the 5% significance level, the hypothesis of no trend is rejected if $|UF_k| > 1.96$. The sequence $x_1, x_2, \ldots, x_n$ is arranged in reverse order, and the above calculation procedure is repeated to obtain the statistic UB_k sequence. When the intersection of two curves (UB_k and UF_k) lies between the significance levels, the intersection is the mutation point.

3.2. Empirical Orthogonal Function (EOF) Method. Empirical Orthogonal Function (EOF) can separate the spatial distribution structure and time-series variation of meteorological element variable fields [30]. The calculation is as follows:

(1) Perform distance leveling on the data and output the data matrix $X_{m\times n}$, where m denotes the number of stations, and n denotes the number of years.

(2) Calculate the cross product of X and X^T to obtain the covariance matrix $C_{m\times m}$.

(3) Compute the characteristic root ($\lambda_1, \lambda_2, \ldots, \lambda_n$) and the eigenvector $V_{m\times m}$ of $C_{m\times m}$, satisfying

$$C_{m\times m} \times V_{m\times m} = V_{m\times m} \times E_{m\times m},$$
$$E = \begin{bmatrix} \lambda_1 & 0 & \cdots & 0 \\ 0 & \lambda_2 & \cdots & 0 \\ \cdots & \cdots & \cdots & \cdots \\ 0 & 0 & \cdots & \lambda_m \end{bmatrix}. \tag{4}$$

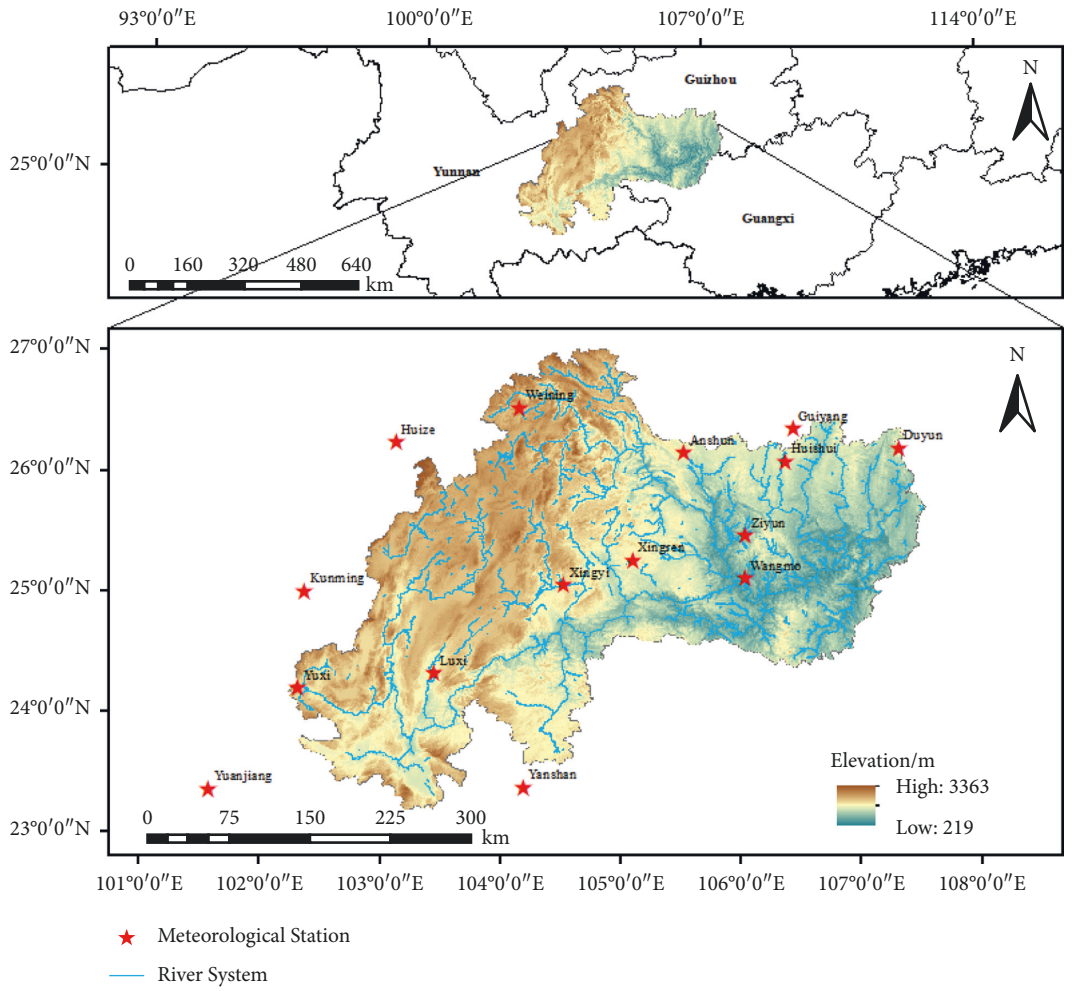

Figure 1: Distribution of main river systems and stations.

Table 1: Definition of extreme temperature index.

	Index	Name	Definition	Unit
			Intensity index	
1	TXx	Extreme T_{max}	The maximum value of daily T_{max} in a year	˚C
2	TNn	Extreme T_{min}	The minimum value of daily T_{min} in a year	˚C
3	DTR	Diurnal temperature range	Average difference between annual daily T_{max} and T_{min}	˚C
			Frequency index	
4	SU25	Summer days	Total number of days with daily T_{max} >25˚C	d
5	FD	Frost days	Total number of days with daily T_{min} <0˚C	d
6	TX90p	Warm days	Annual count of daily T_{max} >90% percentile value	d
7	TN90p	Warm nights	Annual count of daily T_{min} >90% percentile value	d
8	TX10p	Cold days	Annual count of daily T_{max} <10% percentile value	d
9	TN10p	Cold nights	Annual count of daily T_{min} <10% percentile value	d
			Duration index	
10	WSDI	Warm spell duration indicator	Annual count of at least six consecutive days of T_{max} >90% percentile value	d
11	CSDI	Cold spell duration indicator	Annual count of at least six consecutive days of T_{min} <10% percentile value	d

Each characteristic root corresponds to a column of eigenvector values, which is the EOF mode, and $\lambda_1 \geq \lambda_1 \geq \cdots \geq \lambda_m \geq 0$.

(4) Project the EOF onto the original matrix and calculate the time coefficients PC corresponding to the spatial eigenvectors.

Table 2: CMIP5 climate model information.

	Abbreviation of GCM	Model name	Institution/Countries	Resolution (Lon × Lat)
1	BC1	BCC-CSM1.1	BCC/China	128 × 64
2	BNU	BNU-ESM	GCESS/China	128 × 64
3	CaE	CanESM2	CCCMA/Canada	128 × 64
4	CCS	CCSM4	NCAR/USA	288 × 192
5	GF3	GFDL-ESM2G	NOAA GFDL/USA	144 × 90
6	GF4	GFDL-ESM2M	NOAA GFDL/USA	144 × 90
7	IP2	IPSL-CM5A-MR	IPSL/France	144 × 143
8	MI3	MIROC-ESM	MIROC/Japan	128 × 64
9	MI4	MIROC-ESM-CHEM	MIROC/Japan	128 × 64
10	MP1	MPI-ESM-LR	MPI-M/Germany	192 × 96
11	NE1	NorESM1-M	NCC/Norway	144 × 96

Table 3: Results of the extreme temperature trend test.

Index	Kendall's rank correlation method	Spearman rank correlation method	Linear trend regression	Significance test	Trend	Interannual variability °C·(10a)$^{-1}$
TXx	2.99	3	2.81	Significant	Increase	0.14
TNn	4.39	4.98	4.66	Significant	Increase	0.37
DTR	4.58	5.29	5.97	Significant	Decrease	−0.12
SU25	3.42	3.61	3.56	Significant	Increase	2.4
FD	4.3	4.76	4.6	Significant	Decrease	−1.7
TX90p	4.3	4.66	4.88	Significant	Increase	1.1
TN90p	6.37	9.05	9.41	Significant	Increase	2.3
TX10p	1.14	1.17	1.19	Nonsignificant	Decrease	−0.2
TN10p	5.29	6.25	6.52	Significant	Decrease	−1.0
WSDI	4.27	4.61	4.49	Significant	Increase	1.9
CSDI	0.86	0.52	0.08	Nonsignificant	Decrease	−0.2

(5) Calculate the variance contribution of the eigenvectors.

$$R_k = \frac{\lambda_k}{\sum_{i=1}^{m} \lambda_i} \times 100\%. \quad (5)$$

The cumulative variance contribution of the first p vectors is

$$G = \frac{\sum_{i=1}^{p} \lambda_i}{\sum_{i=1}^{m} \lambda_i}. \quad (6)$$

(6) Significance tests were using the North criterion. At the 95% confidence level, the error rate of the eigenvalues is

$$e_j = \lambda_j \sqrt{\frac{2}{n}}. \quad (7)$$

If λ satisfies, $\Delta = \lambda_j - \lambda_{j+1} - e_j \geq 0$, it means that the modes correspond to two eigenvalues that are independent of each other and they are valuable. The characteristic roots are checked in turn, and the error range is calculated. If the error ranges of two adjacent characteristic roots have overlapping parts, the significance of the two characteristic roots does not differ significantly.

3.3. Climate Model Simulation Evaluation Indicators. To better reflect the degree of fit between the simulated and measured values, the following statistics were chosen for this study:

(1) Root mean square error:

$$\mathrm{RMSE} = \sqrt{\frac{1}{n} \sum_{i=1}^{n} (Xoi - Xmi)^2}. \quad (8)$$

(2) Correlation coefficient:

$$r = \frac{\sum_{i=1}^{n} (Xmi - \overline{Xm})(Xoi - \overline{Xo})}{\sqrt{\sum_{i=1}^{n} (Xoi - \overline{Xo})^2 \sum_{i=1}^{n} (Xmi - \overline{Xm})^2}}. \quad (9)$$

(3) Mean absolute error:

$$\mathrm{MAE} = \frac{1}{n} \sum_{i=1}^{n} |Xmi - Xoi|. \quad (10)$$

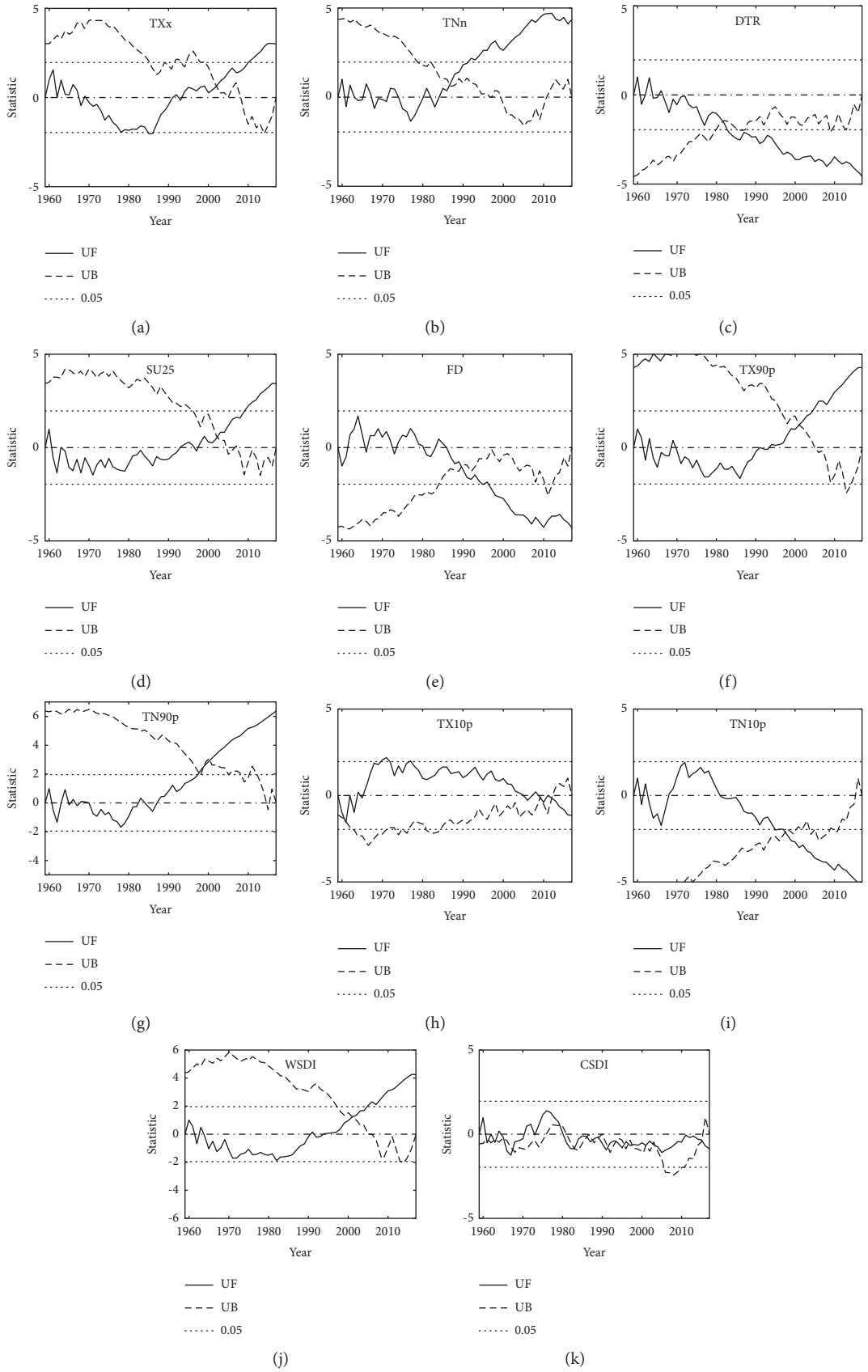

Figure 2: M-K mutation trend test results.

(4) Nash efficiency coefficient:

$$\mathrm{NSE} = 1 - \frac{\sum_{i=1}^{n} (Xoi - Xmi)^2}{\sum_{i=1}^{n} (Xoi - \overline{Xo})^2}. \quad (11)$$

(5) Trend error

There is an error between the linear trend of the simulated series and the measured series:

where X_{mi} is the simulated value, X_{oi} is the measured value, and n is the total number of time series.

3.4. Composite Rating Metrics. Composite Rating Metrics (M_R) is a method to judge the consistency and get a composite ranking based on the ranking of each rating index [31]. In this study, multiple statistical indicators of annual and monthly scale simulated and measured series are calculated separately, and then each model is ranked according to the merit of the fit, and the best climate model is selected by judging the comprehensive simulation ability of each model.

$$MR = 1 - \frac{1}{nm} \sum_{i=1}^{n} ri, \quad (12)$$

where m is the number of models involved in the evaluation, n is the number of indexes used for the evaluation, and r_i is the overall ranking of each model ($i = 1,2,...,11$), and the model with the best simulation ability has a r_i value of 1. The closer the M_R is to 1, t the better the model simulation is.

4. Results

4.1. Temporal Variation Characteristic

4.1.1. Variation Tendency. The trend test results of the change of the mean extreme temperature indices in the basin for the past 59 years are shown in Table 3. The significance level was selected as 0.05, and the trend was obtained by combining the three methods of testing. The results of the three methods are consistent. Therefore, they have certain reliability. All indices passed the significance trend test at the 0.05 confidence level except for the cold days (TX10p) and the cold spell duration indicator (CSDI). Overall, the warm-related indices all showed an increasing trend.

To further analyze the trend changes of the extreme temperature indices in different years, the M-K trend test was adopted in this study and used to calculate the UF, thus analyzing the changes of each index in different years. The results of the analysis are shown in Figure 2. Most indices tend to change significantly in trend after 2000, with large fluctuations in the 1980s and 1990s. TXx, TNn, TX90p, and TN90p all showed an increasing trend around 1990, while DTR, FD, and TN10p all showed a decreasing trend and fluctuated greatly in the 1960s. SU25 and WSDI showed a decreasing trend at first and then an increasing trend.

Table 4: Variance contribution rate and North significance test results of the first four modes of extreme temperature index.

	TXx				TNn			
	EOF1	EOF2	EOF3	EOF4	EOF1	EOF2	EOF3	EOF4
R (%)	42	15	12	9	54	16	8	5
G (%)	42	57	69	78	54	70	78	84
Δ	4	0	0	0	13	2	1	0
	DTR				SU25			
	EOF1	EOF2	EOF3	EOF4	EOF1	EOF2	EOF3	EOF4
R (%)	54	18	9	5	54	14	8	6
G (%)	54	71	80	85	54	68	75	81
Δ	1	0	0	0	988	112	0	34
	FD				TX90p			
	V1	V2	V3	V4	V1	V2	V3	V4
R (%)	63	17	7	5	66	11	6	5
G (%)	63	80	87	91	66	77	83	89
Δ	187628	38288	18025	−11414	172	14	−2	6
	TN90p				TX10p			
	EOF1	EOF2	EOF3	EOF4	EOF1	EOF2	EOF3	EOF4
R (%)	71	13	6	3	52	19	9	5
G (%)	71	83	89	92	52	71	79	85
Δ	351	35	13	5	31	9	2	1
	TN10p				WSDI			
	EOF1	EOF2	EOF3	EOF4	EOF1	EOF2	EOF3	EOF4
R (%)	57	12	7	6	59	12	8	6
G (%)	57	69	76	83	59	71	78	84
Δ	73	5	−1	2	571	29	7	18
	CSDI							
	EOF1	EOF2	EOF3	EOF4				
R (%)	33	20	13	10				
G (%)	33	52	66	76				
Δ	36	15	3	18				

4.1.2. Mutation Test. The results of the extreme temperature mutation trend test are shown in Figure 2, when there were multiple intersections in the M-K mutation test, the mutation points were determined by combining the results of the sliding t-test. The intersection of UF and UB curves of TXx at the confidence interval is 2002, indicating that TXx mutated around 2002. TNn mutated around 1986, DTR mutated around 1981, SU25 may have mutated around 2002, and FD mutated around 1990. The mutation time of TX90p, TN90p, and TX10p was 2001, 1997, and 2012, respectively. TN10p was mutated around 1994, and WSDI was mutated in 2002. The trend of CSDI is not significant, and UF and UB curves have multiple intersection points within the confidence interval. Combined with the sliding t-test results, the

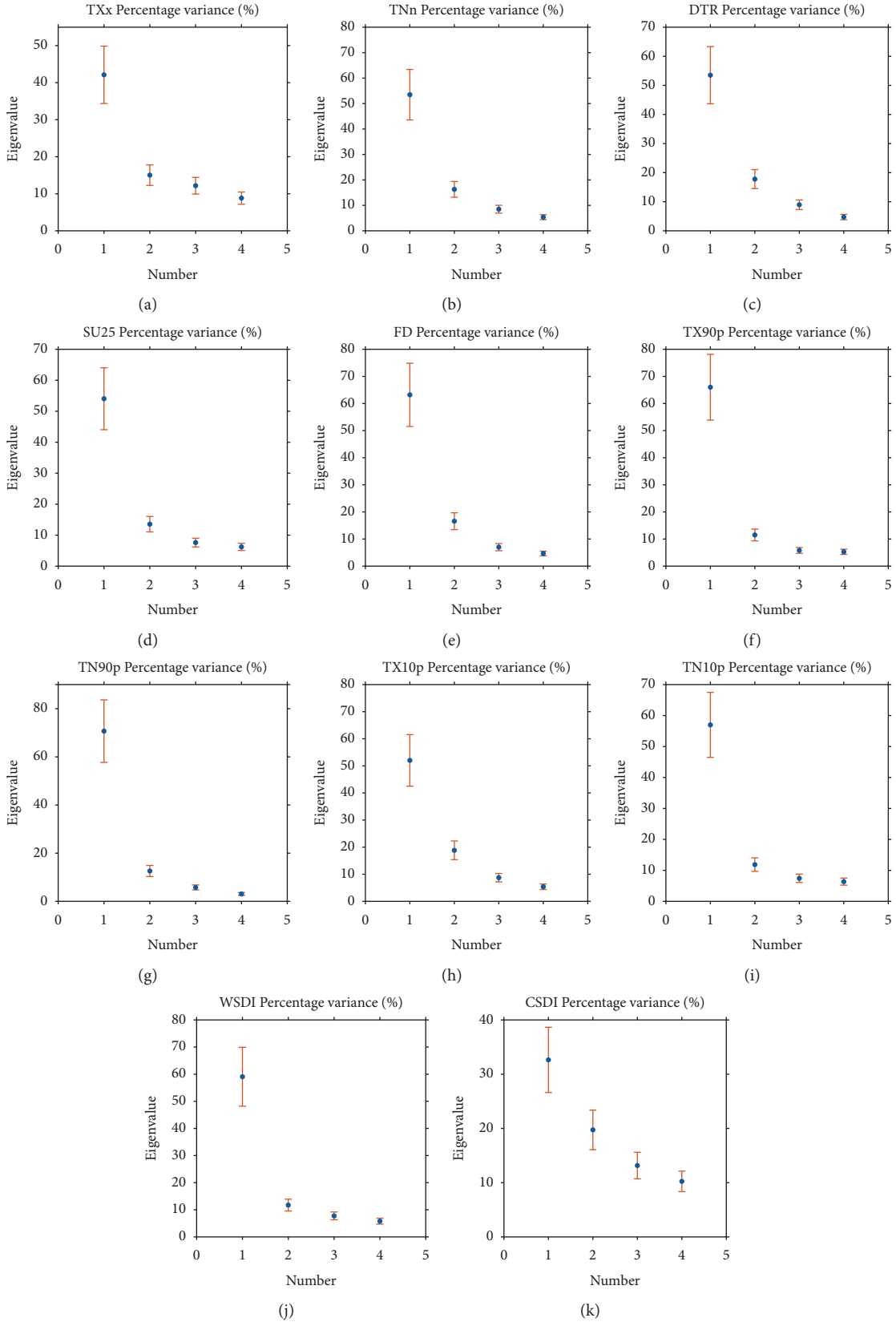

Figure 3: Characteristic root of extreme temperature and 95% confidence error.

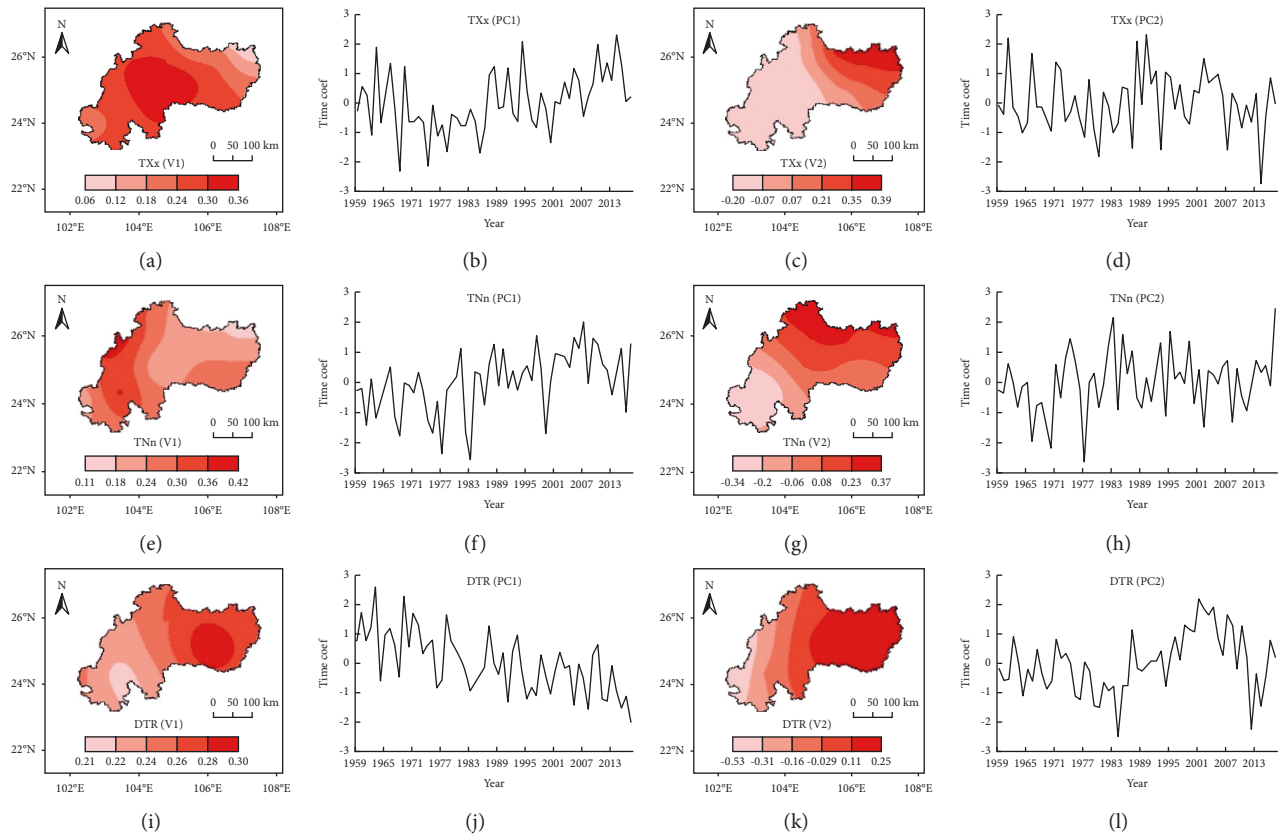

Figure 4: The first and second eigenvectors and their time coefficients of extreme temperature intensity index.

mean value has no significant jump, and there is no mutation point. Overall, TNn and DTR had a mutation in the 1980s. FD, TN90p, and TN10p had mutations in the 1990s. TXx, SU25, and TX90p had mutations around 2000.

4.2. Spatial Variation characteristics. The variance contribution rate, cumulative variance contribution rate, and North test results of the EOF for the first four modes decomposed from the extreme temperature are shown in Table 4. The first three modes of TX90p and the first two modes of TN90p and WSDI passed the test, and the first four modes of the remaining indices passed the test. Combining the extreme temperature characteristic roots and 95% confidence error (Figure 3), the first two more significant modes and their time coefficients were selected for analysis in terms of the intensity index (TXx, TNn, and DTR), frequency index (SU25, FD, TX90p, TN90p, TX10p, and TN10p), and duration index (WSDI, CSDI) of the extreme temperature.

4.2.1. Intensity Indices. As shown in Figure 4, the first eigenvectors of the extreme temperature intensity indices are all positive, indicating that the trend of extreme temperature intensity change in the basin is basically the same, but the high-value centers are different. The high-value center of TXx (V1) is distributed in the mid-basin region and decreases in all directions, and the high-value center of TNn (V1) is in the upper reaches of the watershed. It can be found that the temporal coefficients of TXx(PC1) and TNn(PC1) increase significantly from 1959 to 2017, so both extreme maximum and extreme minimum temperatures show increasing trends in the past 59 years. The areas of high values of DTR (V1) are distributed in the lower part of the basin, and the amount of change in the areas of high values is greater than the change in other areas. Combined with the temporal coefficients, the temporal coefficients from 1969 to 2017 show a significant decreasing trend. Therefore, the diurnal temperature range (DTR) is significantly lower. The second eigenvectors are all positive and negatively distributed, and the negative areas are distributed in the southwest of the watershed. The negative areas of TXx (V2) and DTR (V2) are larger, and the high-value center of TXx (V2) is in the northeast region, decreasing along the southwest. The high-value center of TNn (V2) is in the northern region, decreasing along the south. The high-value center of DTR (V2) is negative and located in the southwest region, decreasing along the east. The positive and negative distribution indicated that the TXx (V2), TNn (V2), and DTR (V2) represent two types of distribution, that is, the positive regions with opposite trends of negative regions.

4.2.2. Frequency Indices. As shown in Figure 5, the first eigenvectors of FD (V1), TX10p (V1), and TN10p (V1) are all positive, indicating that the spatial variation trends of FD, TX10p, and TN10p are basically the same. The other eigenvectors are positive and negative, but most regions are

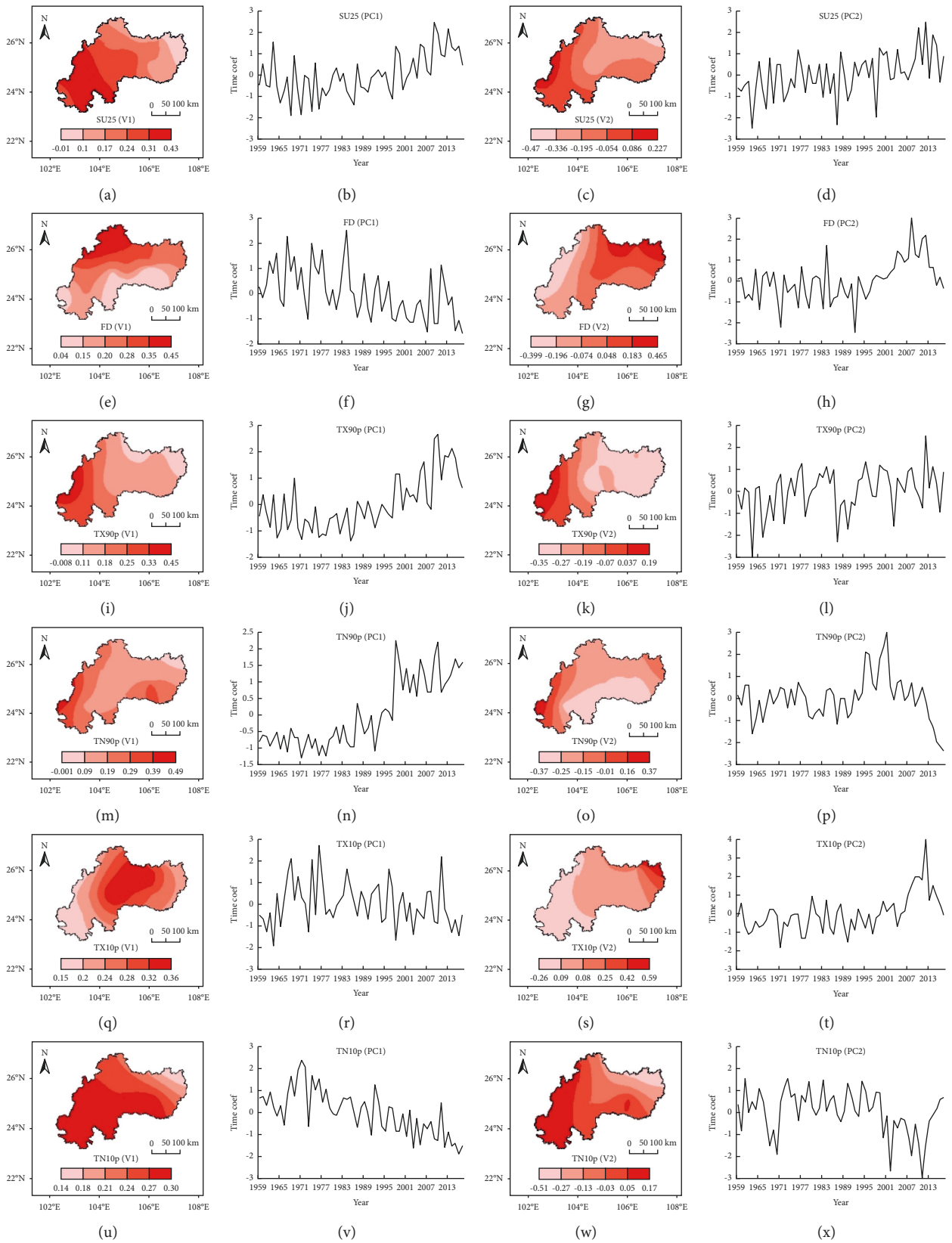

Figure 5: The first and second eigenvectors and their time coefficients of extreme temperature frequency index.

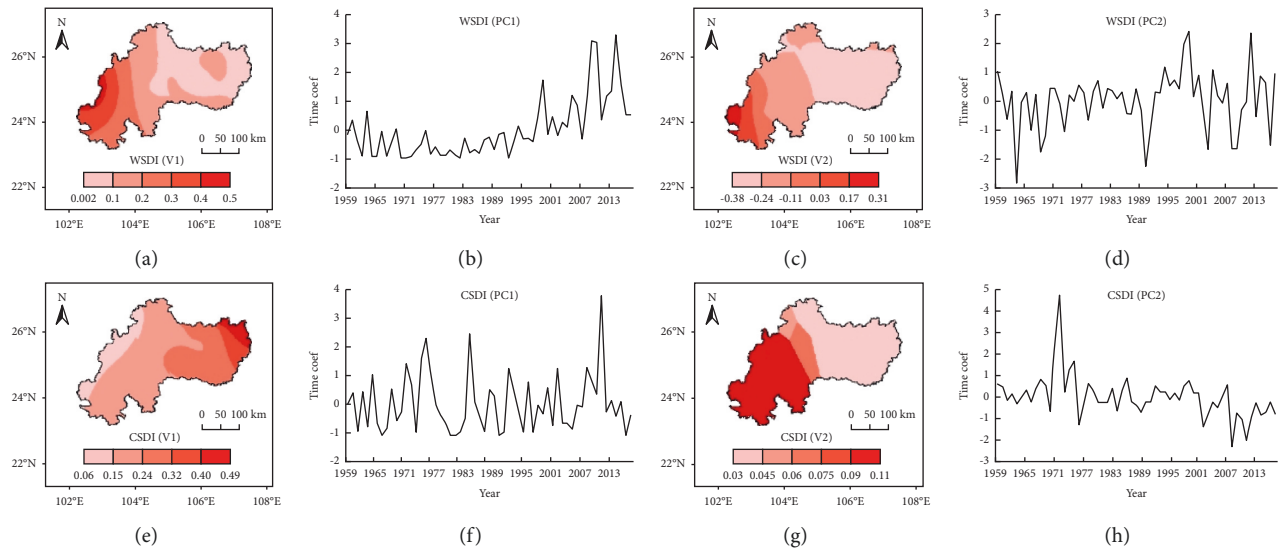

Figure 6: The first and second eigenvectors and their time coefficients of extreme temperature duration index.

positive, with small differences in trends. The component values of FD (V1) are distributed along the south-north, with the center of high values located in the north of the basin and decreasing to the south. The center of high values of TX10p (V1) is located in the middle part of the watershed, with the component values decreasing along the surrounding area. The values of the other eigenvectors all change along the southwest or northeast direction, but the locations of the high-value centers are different. The component values of the second eigenvector were increasing or decreasing along the southwest-northeast direction, and all of them were positively and negatively distributed. For example, the component value of SU25 (V2) tends to decrease along the southwest to northeast direction, while that of TX10p (V2) tends to increase. The indices with more negative areas of component values were SU25 (V2), TX90p (V2), and TN90p (V2). The positive high-value center of TN90p (V2) is located in the southwest, and the negative high-value center is located in the southeast part, with an inverse distribution pattern; that is, southwest increased, and northeast decreased, or southwest decreased and northeast increased distribution pattern.

As can be seen from the time coefficients, SU25 (PC1) and SU25 (PC2) have relatively smooth trend changes, and both show an increasing trend after 2007. FD (PC1) has an overall decreasing trend with four significant fluctuations, showing an upward and then a downward trend, while FD (PC2) has relatively stable changes from 1964 to 1996 and a significant upward trend from 1997 to 2012. TX90p (PC1) has a decreasing and then increasing trend with the alternation point near 1984. TX90p (PC2) has a significant fluctuation between 1986 and 1998, while it has an increasing trend before 1986 and was relatively stable after 1998. TN90p (PC1) changed smoothly until 1986, showed a clear upward trend after 1986, and gradually stabilized after 2002. TN90p (PC2) showed an upward trend after 1990 and a downward trend after 2003. TX10p (PC1) showed a fluctuating change, with an upward trend from 1964 to 1971. TX10p (PC2) showed a relatively stable change until 2004 and an increasing trend after 2004. TN10p (PC1) showed a decreasing trend, TN10p (PC2) showed two significant fluctuations in 1965–1977 and 2000–2015, and it was relatively stable in 1978–1999.

4.2.3. Duration Indices. As shown in Figure 6, the trends of WSDI and CSDI reflected by the first eigenvector are basically the same in space. The center of high value of WSDI (V1) is in the southwest of the watershed, decreasing along the northeast, while the center of high value of CSDI (V1) is in the northeast part, decreasing along the west. The time coefficients show that WSDI (PC1) changed smoothly until 1992 and then showed a clear upward trend, and WSDI (PC2) started to rise around 1992 and decreased after 2000. The second eigenvector WSDI (V2) has a positive and negative type of distribution, with positive values in the southwest and negative values in the northeast representing two types of distribution; that is, there is a distribution pattern of WSDI in the watershed increased in the southwest and decreased in the northeast or decreased in the southwest and increased in the northeast in different years. While CSDI (V2) is all positive, it showed spatial consistency overall. WSDI (V2) and CSDI (V2) correspond to time coefficients WSDI (PC2) and CSDI (PC2) with different change characteristics. WSDI (PC2) changed smoothly before 1990 and showed a trend of rising and then fell from 1991 to 2010. CSDI (V2) changed relatively smoothly, with one fluctuation in 1971–1977, and the eigenvector distribution type was significant in 1972.

4.3. Model Selection. As stated in the study area section, there is a Longtan Control Project built in the basin, and preparatory construction work such as resettlement was carried out in the 1990s, and the environment of the watershed has changed significantly due to human activities. The study of the temporal variation characteristics of the

Table 5: The evaluation statistics by each climate model simulated at Luxi Station.

			BC1	BNU	CaE	CCS	GF3	GF4	IP2	MI3	MI4	MP1	NE1
Annual scale	T_{max}	RMSE	1.62	1.70	1.57	1.43	1.43	1.65	1.43	1.52	1.53	1.60	1.68
		R	0.18	−0.04	0.03	0.29	0.23	−0.10	0.10	0.07	0.42	−0.17	−0.02
		MAE	1.34	1.50	1.18	1.03	1.07	1.27	1.10	1.22	1.23	1.34	1.43
		NSE	−0.84	−1.03	−0.73	−0.45	−0.44	−0.91	−0.44	−0.63	−0.65	−0.79	−0.99
		TE	0.12	0.18	0.08	0.36	0.28	0.00	0.18	0.41	0.28	0.03	0.03
	T_{min}	RMSE	2.85	2.74	2.92	3.03	2.73	2.88	2.89	2.84	2.72	3.01	3.06
		R	0.21	0.18	0.24	−0.18	0.01	0.28	0.32	0.19	−0.15	0.10	0.17
		MAE	2.19	2.07	2.13	2.44	2.13	2.23	2.16	2.23	2.12	2.44	2.35
		NSE	−0.34	−0.23	−0.40	−0.50	−0.22	−0.36	−0.37	−0.32	−0.22	−0.49	−0.54
		TE	0.08	0.06	0.06	0.41	0.16	0.18	0.34	0.60	0.50	0.47	0.40
Monthly scale	T_{max}	RMSE	2.77	2.76	2.73	2.76	2.73	2.75	2.71	2.77	2.81	2.77	2.77
		R	0.80	0.79	0.80	0.80	0.80	0.79	0.79	0.78	0.84	0.78	0.80
		MAE	2.34	2.30	2.28	2.29	2.28	2.30	2.24	2.32	2.37	2.32	2.31
		NSE	0.40	0.40	0.42	0.09	0.42	0.41	0.43	0.40	0.38	0.40	0.40
		TE	0.00	0.01	0.00	0.40	0.01	0.00	0.01	0.01	0.03	0.00	0.00
	T_{min}	RMSE	2.55	2.51	2.39	2.50	2.45	2.50	2.55	2.49	2.52	2.41	2.46
		R	0.92	0.92	0.93	0.92	0.93	0.92	0.92	0.92	0.92	0.93	0.92
		MAE	1.96	1.95	1.82	1.92	1.93	1.96	1.96	1.96	1.95	1.92	1.92
		NSE	0.84	0.85	0.86	0.85	0.85	0.85	0.84	0.85	0.85	0.86	0.85
		TE	0.02	0.01	0.02	0.03	0.02	0.02	0.01	0.02	0.00	0.03	0.01

Table 6: The evaluation statistics by each climate model simulated at Xingren Station.

			BC1	BNU	CaE	CCS	GF3	GF4	IP2	MI3	MI4	MP1	NE1
Annual scale	T_{max}	RMSE	1.63	1.43	1.51	1.52	1.57	1.46	1.41	1.62	1.55	1.42	1.60
		R	0.10	0.16	0.11	0.07	−0.09	0.19	−0.05	−0.31	0.26	0.02	−0.10
		MAE	1.32	1.13	1.27	1.28	1.25	1.22	1.14	1.26	1.22	1.12	1.30
		NSE	−1.87	−1.21	−1.46	−1.48	−1.64	−1.31	−1.16	−1.84	−1.59	−1.17	−1.78
		TE	0.09	0.06	0.16	0.16	0.20	0.06	0.14	0.12	0.03	0.08	0.12
	T_{min}	RMSE	1.96	1.81	1.96	1.65	1.76	2.13	1.98	2.03	2.06	1.97	1.76
		R	−0.06	0.10	0.03	0.30	0.10	−0.25	−0.01	−0.34	−0.11	−0.06	0.09
		MAE	1.65	1.39	1.52	1.41	1.42	1.66	1.49	1.59	1.53	1.69	1.32
		NSE	−0.84	−0.56	−0.83	−0.30	−0.48	−1.16	−0.87	−0.96	−1.02	−0.85	−0.48
		TE	0.51	0.44	0.35	0.73	0.49	0.93	0.81	1.22	0.86	0.60	0.84
Monthly scale	T_{max}	RMSE	2.77	2.76	2.73	2.76	2.73	2.75	2.71	2.77	2.81	2.77	2.77
		R	0.80	0.79	0.80	0.80	0.80	0.79	0.79	0.78	0.84	0.78	0.80
		MAE	2.34	2.30	2.28	2.29	2.28	2.30	2.24	2.32	2.37	2.32	2.31
		NSE	0.40	0.40	0.42	0.09	0.42	0.41	0.43	0.40	0.38	0.40	0.40
		TE	0.00	0.01	0.00	0.40	0.01	0.00	0.01	0.01	0.03	0.00	0.00
	T_{min}	RMSE	2.55	2.51	2.39	2.50	2.45	2.50	2.55	2.49	2.52	2.41	2.46
		R	0.92	0.92	0.93	0.92	0.93	0.92	0.92	0.92	0.92	0.93	0.92
		MAE	1.96	1.95	1.82	1.92	1.93	1.96	1.96	1.96	1.95	1.92	1.92
		NSE	0.84	0.85	0.86	0.85	0.85	0.85	0.84	0.85	0.85	0.86	0.85
		TE	0.02	0.01	0.02	0.03	0.02	0.02	0.01	0.02	0.00	0.03	0.01

extreme temperature indices revealed that, in the Longtan watershed, most of the extreme indices changed abruptly in the 1990s and 2000s, and the 30-year time series was sufficient for the simulated evaluation of climate models [32–35]. Therefore, the period from 1961 to 1990 with relatively little climate change was used as the simulation period for model evaluation in this study. Based on the temperature observation data of the Longtan watershed from 1961 to 1990, the root mean square error (RMSE), correlation coefficient (R), mean absolute error (MAE), Nash efficiency coefficient (NSE), and trend error (TE) of the simulated maximum and minimum temperatures of each climate model at monthly and annual scales were used as evaluation indicators, and the simulation effects of 11 climate models were evaluated by comprehensive rating metrics. According to the analysis of the spatial and temporal characteristics of extreme temperatures in the previous sections, most of the indices show a distribution of more in the southwest and less in the northeast or more in the southwest and less in the northeast. Therefore, the Luxi station in the southwest and Xingren station in the northeast are chosen as the representative station for showing the simulations of 11 climate models. The evaluation statistics by each climate model simulated at Luxi and Xingren stations are shown in Table 5 and Table 6, respectively. The composite rating results of each model are shown in Table 7.

Table 7: Results of the composite rating metrics of each climate model.

Station	BC1	BNU	CaE	CCS	GF3	GF4	IP2	MI3	MI4	MP1	NE1
Luxi	0.35	0.40	0.63	0.47	0.64	0.47	0.50	0.37	0.43	0.38	0.38
Xingren	0.33	0.52	0.51	0.54	0.59	0.31	0.33	0.26	0.47	0.52	0.62

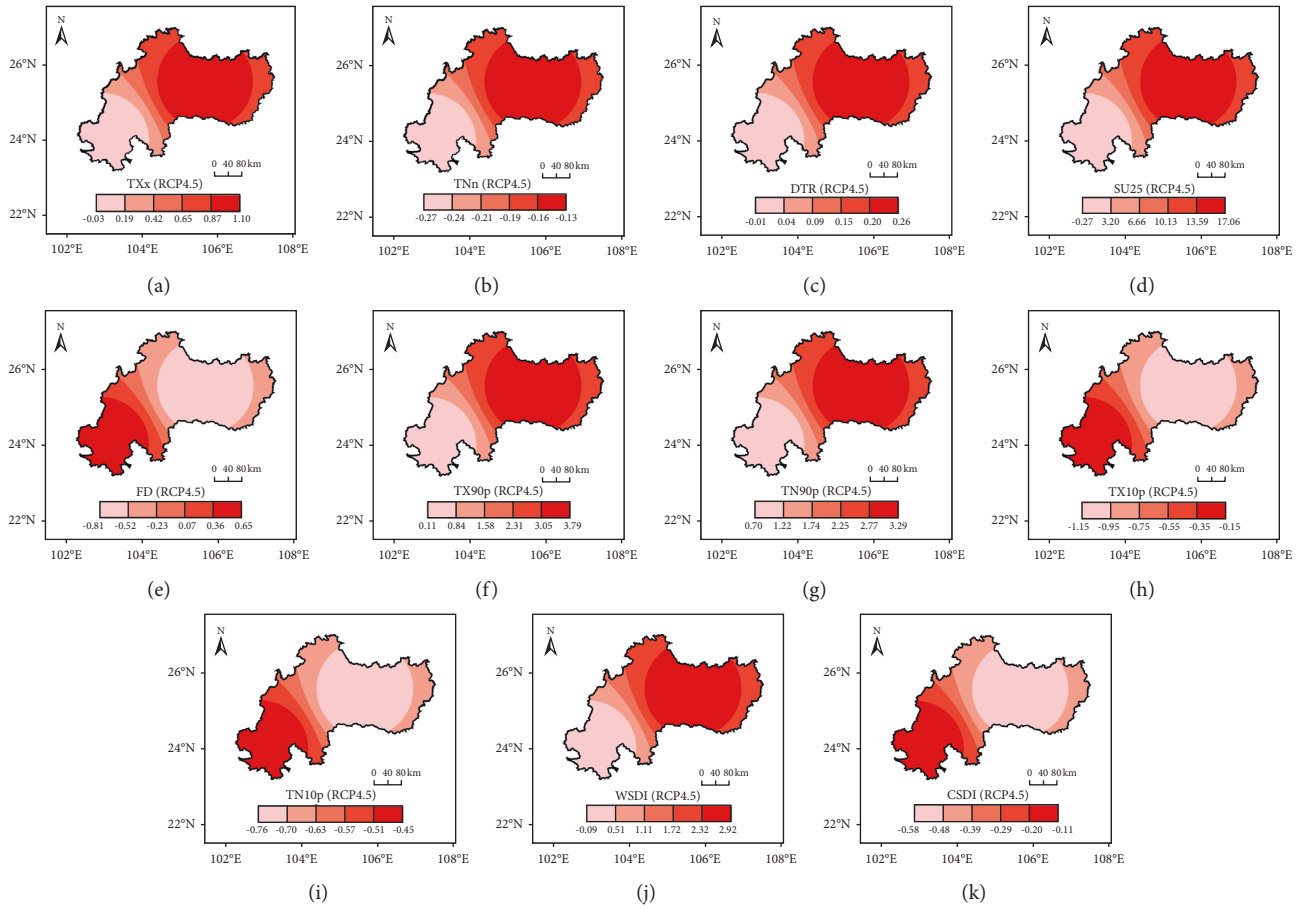

Figure 7: Spatial distribution of interdecadal variability of temperature extremes for 2021–2050 under the RCP4.5.

At Luxi station, except for CCS, MP1, and NE1, most climate models simulate annual-scale maximum and minimum temperatures within a root mean square error of 3. The mean absolute error is within 2.5°C, and the MI3 model had the largest temperature trend error. At the monthly scale, the root mean square error of the simulations of each climate model is between 2.39 and 2.81, and the mean absolute error is within 2.5°C. The variation temperature trend of the simulated minimum temperature of CCS is opposite to the measured trend, and the trend error is large compared with other models. In a comprehensive evaluation, the GF3 model scored higher than other climate models at Luxi station. At the Xingren station, the root mean square error of each model at the annual scale ranged from 1.41 to 2.13, and the mean absolute error was less than 2°C. On the monthly scale, the simulation results of NE1 are mostly better than other models. The comprehensive evaluation results show that the NE1 climate model simulated the temperature of the Xingren station best. In summary, the evaluation results are as follows: the GF3 model performs best at Luxi station, and NE1 simulates best at Xingren station. Therefore, the GF3 model is selected at the Luxi station, and the NE1 model is selected at the Xingren station to evaluate the future temperature change.

4.4. Future Trends. Figures 7 and 8 show the spatial distribution of interdecadal changes in each extreme temperature index predicted by the selected models for 2021–2050 under the RCP4.5 and RCP8.5, respectively. Under the RCP4.5 scenario, the multiyear average of TXx will increase by 2.1°C, and the multiyear average of TNn will increase by 0.4°C relative to the reference period 1961–1990. In the basin, the TXx showed a decreasing trend in a small part of the southwest, but with little interannual variation, and an increasing trend in the middle and lower reaches of the basin with relatively large interannual variation and an interannual tendency rate of 0.19–1.10°C·(10a)$^{-1}$. The TNn showed a

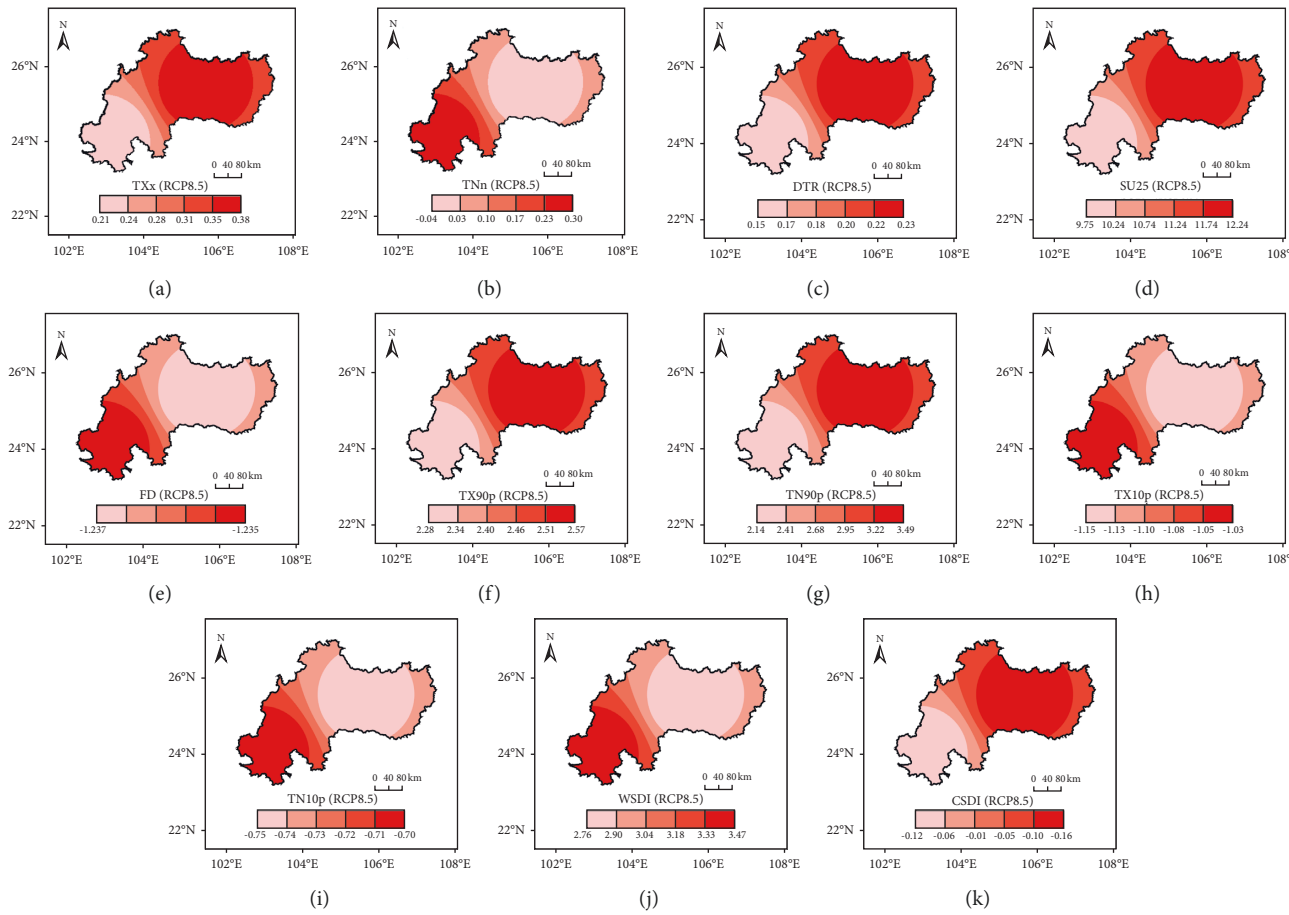

Figure 8: Spatial distribution of interdecadal variability of temperature extremes for 2021–2050 under the RCP8.5.

decreasing trend in the basin, and from the interannual variation, the interannual variation of the TNn is lower than that of the TXx, and the interannual variation in the middle and lower reaches is greater than that in the upper reaches. FD changes in an opposite trend in the upstream and downstream, and CSDI does not change significantly. The other warm-related indices (SU25, TX90p, TN90p, and WSDI) showed an increasing trend in most areas of the basin, and the cold-related indices (TX10p, TN10p) all showed a decreasing trend. Under the RCP8.5 scenario, the TXx will increase by 2.0°C, and the TNn will increase by 0.3°C relative to the base period 1961–1990. In the basin, the TXx showed an increasing trend, and the interannual variation is greater in the downstream area than in the upstream area. The TNn showed an increasing trend except for some areas in the northeast, which showed a decreasing trend. CSDI does not change significantly. All other warm-related indices showed increasing trends, and all cold-related indices showed decreasing trends. The comparison of the two scenarios revealed that the TXx showed an increasing trend in most regions, but there were differences in the spatial distribution of interannual variation, and the interannual variation of the TXx was larger in most regions under the RCP4.5 scenario than under the RCP8.5 scenario. The TNn showed a decreasing trend under the RCP4.5 scenario and an increasing trend in most regions under the RCP8.5 scenario, and there is a large interannual variation under the RCP8.5 scenario. In summary, the extreme temperature in the watershed may show a warming trend in 2021–2050.

Figures 9 and 10 show the spatial distribution of the multiyear averages of each extreme temperature index in the watershed predicted by the selected models for 2021–2050 under the RCP4.5 and RCP8.5, respectively. Under the RCP4.5 scenario, TXx, SU25, TN90p, TX10p, and CSDI showed a spatial characteristic of high northeast and low southwest, while the other indices showed a distribution of low northeast and high southwest. The spatial distributions of TXx and TNn indices under the two scenarios are slightly different. The region of TXx greater than 33.7°C is larger in RCP8.5 than in RCP4.5, and the TXx reaches 34.4°C under RCP8.5, while the maximum value of TXx is 33.9°C under RCP4.5. Most areas of TNn under RCP4.5 are above −3.6°C. And the spatial distribution of TNn under the RCP8.5 scenario did not differ significantly, all above −3.6°C. The prediction results reveal that there is a warming trend of the extreme temperature in the next 30 years, and the risk of extreme high temperature may exist in the downstream areas of the basin in the future. Under the RCP4.5 scenario, the TXx index increases interannually in the downstream region, increasing the risk of extreme high temperature. The interannual variation of the extreme low temperature in the northeastern part of the watershed weakens, and the risk of

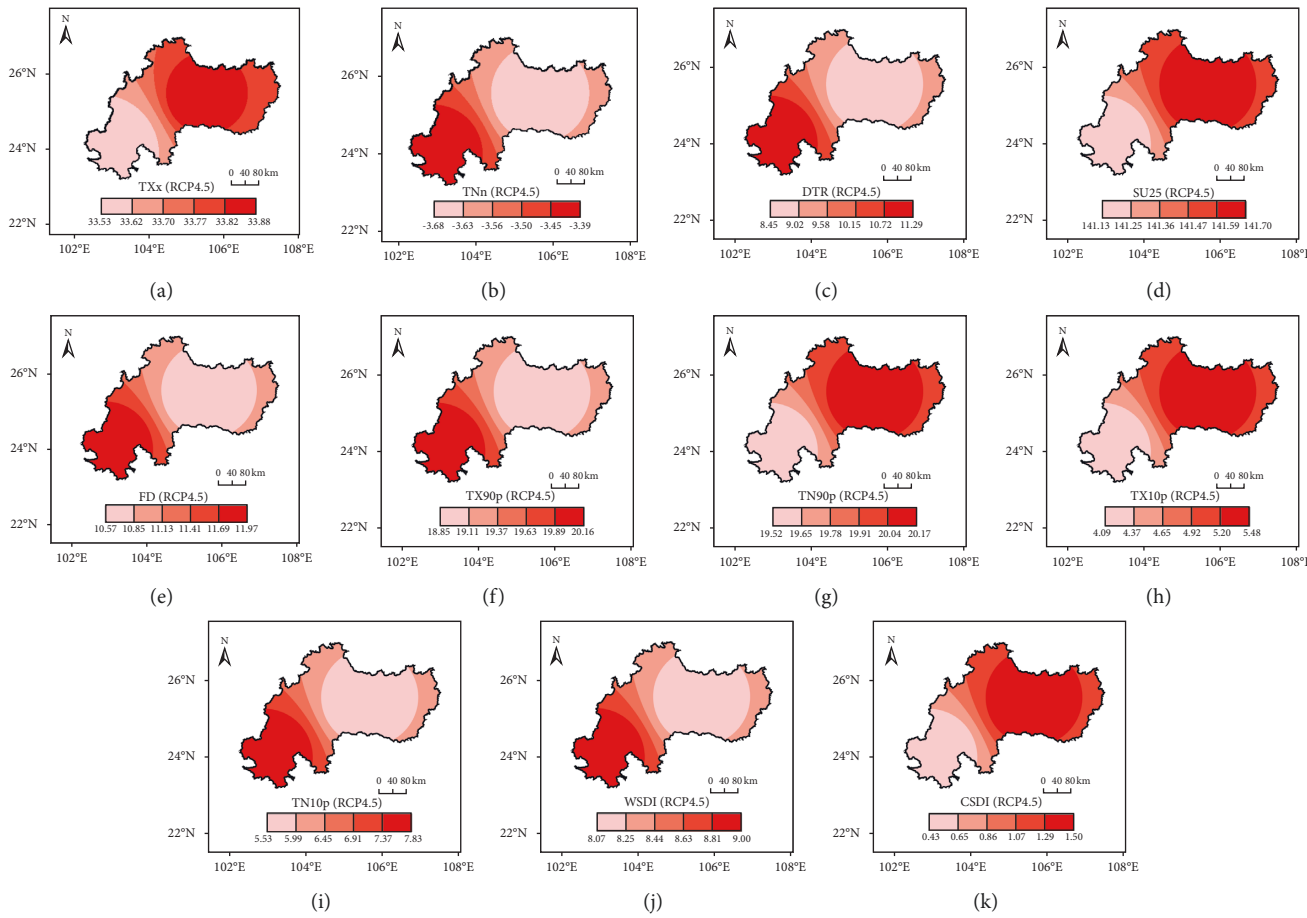

Figure 9: Spatial distribution of temperature extremes for 2021–2050 under RCP4.5.

extreme low temperatures may decrease. Under the RCP8.5 scenario, the interannual variability of TXx increases in the northeastern region, and the extreme high-temperature risk likewise increases.

5. Discussion

In this study, the trends of extreme temperature in the Longtan watershed from 1959 to 2017 were comprehensively analyzed by using several extreme temperature indices, and the results of the study showed that the extreme temperature changes showed a warming trend, which is generally consistent with similar studies in other regions. For example, the results of Supari et al. [12] showed that the cold days (TX10p) and cold nights (TN10p) both showed decreasing trends in Indonesia, the warm days (TX90p) and warm nights (TN90p) both showed increasing trends, and all other extreme temperature indices showed warming trends. In Malaysia, most of the extreme warm indices increased significantly, and the warm night (TN90p) increased significantly at more than 75% of the stations [36]. Similar studies have been learned in Korea [37], New Zealand [13], and globally [38], where extreme temperature indices indicate a warming trend in extreme temperature changes. However, the extreme temperature indices change at different rates in different regions. Shen et al. [4] found that the annual T_{max} increased by $0.28^{\circ}C\cdot(10a)^{-1}$ in North Central China, while this study found that the TXx increased by $0.14^{\circ}C\cdot(10a)^{-1}$ in the Longtan watershed, which increased slowly compared with North Central China. Therefore, it is necessary to study the temperature extremes in different regions. In addition, the extreme temperature indices with significant trends all changed abruptly and mainly occurred in the 1980s, 1990s, and after the 2000s, which was generally consistent with the findings of Wang et al. [39]. Empirical orthogonal function (EOF) analysis is a common spatio-temporal analysis method in atmospheric science. Jia [40] used this method to study the characteristics of spatio-temporal distribution of high and low-temperature climate variables in Liaoning Province, and the results showed that the first mode reflected a good spatial consistency of extreme temperature variation patterns in Liaoning Province. In Chongqing, Guo et al. [41] found from the EOF decomposition results that the first mode was the main type of spatial variation of extreme maximum temperature in Chongqing in summer, and the spatial distribution of extreme maximum temperature had a good consistency. These results are all similar to the conclusion that the first eigenvectors of all indices in this study reflect the general consistency of the trends in the spatial variation of each index, indicating a good spatial consistency of the extreme temperature variation across locations. In summary, the

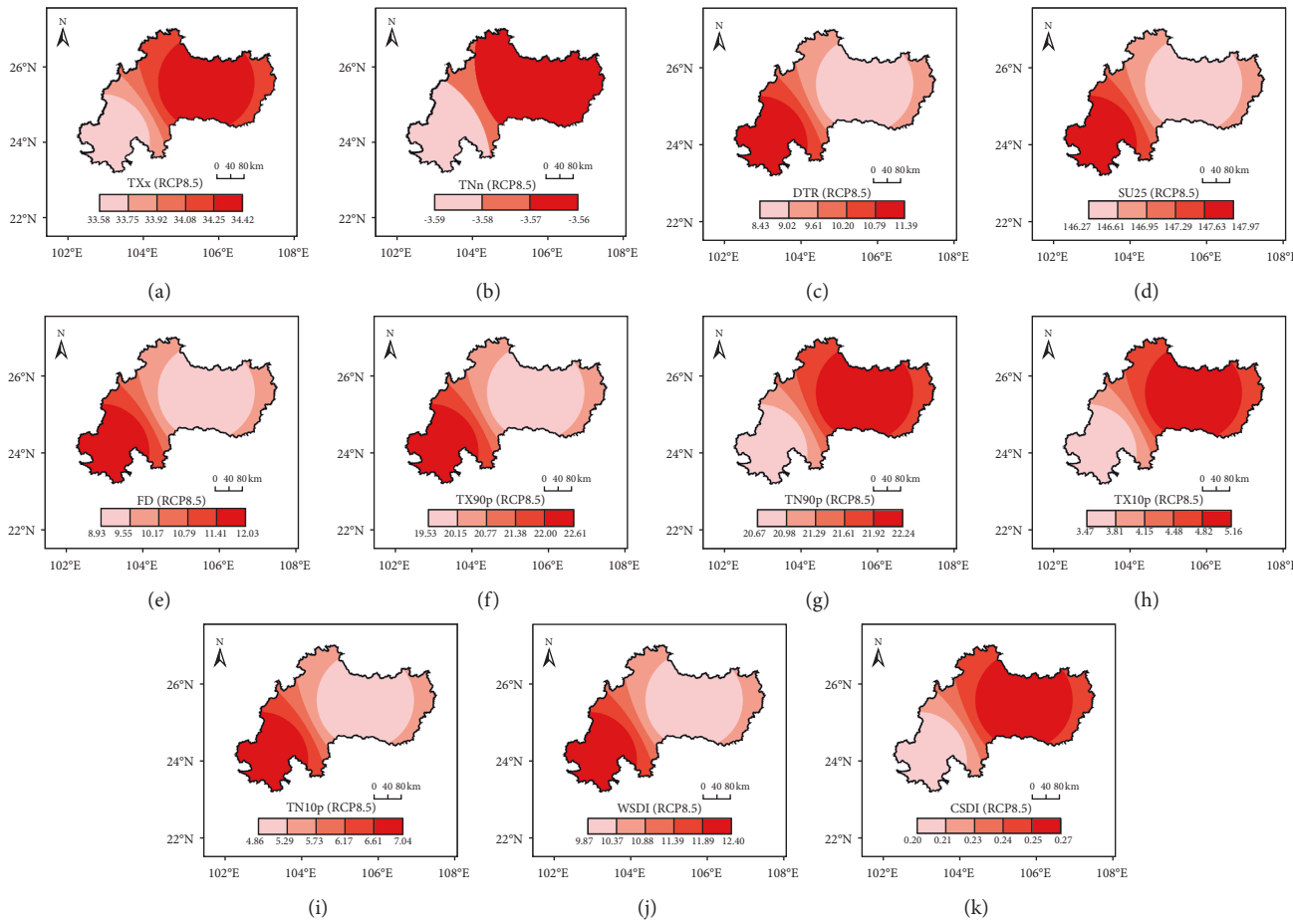

Figure 10: Spatial distribution of temperature extremes for 2021–2050 under RCP8.5.

trend of extreme temperature in the Longtan watershed is consistent with the trend of extreme temperature in other regions, and the spatial distributions all have good spatial consistency.

The results of the climate model evaluation found that the climate models selected by the comprehensive rating metrics for the simulation effect were different at different stations in the basin, which may be due to the different geographical characteristics among the different stations, GF3 fitted the temperature at Luxi station best and NE1 simulation at Xingren station the best. Under the RCP4.5 and RCP8.5 emission scenarios, an increasing trend of the extreme warm index and a decreasing trend of the extreme cold index are predicted for Shanghai from 2021 to 2030 [42]. This result is generally consistent with the predicted warming trend of extreme temperatures in the Longtan watershed for the next 30 years in this study. However, due to the different geographical characteristics of the region, the rate of change of extreme temperature indices and their trends may differ in different areas, and the results show that there may be a risk of extreme high temperature in the downstream area. Xiao et al. [43] found that the TXn index increases most significantly in the eastern part of the Han River basin in the next 40 years under the RCP4.5 emission scenario. Therefore, further attention to the influence of regional characteristics on future temperature extremes is needed.

There is evidence that extreme temperature events may hurt human life. For example, extreme heat and cold temperatures are positively associated with respiratory mortality in China [44]. Global warming and extreme temperature events may also have adverse ecological impacts; for example, increased temperature extremes may cause the uneven distribution of water resources spatially and seasonally [42]. In addition, Haile et al. [45] found that temperature extremes may hurt the production of crops such as rice and corn. The contribution of urbanization to temperature warming trends cannot be ignored, there was a significant urbanization impact on the occurrences of extremely warm and cold nights, and the effect of urbanization contributed about 12.7% to the increasing trend of warm nights and 29% to the decreasing trend of cold nights in Beijing [46]. Nowadays, China's urbanization process is accelerating, and related departments should pay attention to the impact of urbanization on temperature extremes in the process of urbanization, so that the extreme temperatures will not cause harm to people's production and life. It also recommended that policymakers and managers in the watershed fully consider the negative impacts of extreme temperature increases in future urban construction, increase

urban greenery coverage, and establish safe public drinking water areas to reduce the hazards associated with the occurrence of extreme heat events.

The innovation of this study is to use more extreme temperature indices and more mathematical methods to study the extreme temperature variation characteristics of the Longtan basin, so that the research results are clearer and can reflect the extreme temperature variation characteristics of the Longtan watershed more comprehensively. One of the advantages of the proposed framework is that this study does not only study the spatial and temporal distribution characteristics of regional extreme temperatures, but also combine the historical spatial and temporal characteristics of extreme temperatures and use representative stations to further study the future extreme temperature changes, which can better provide data support for the prevention of various extreme temperature disasters in the future.

However, there are still some shortcomings to be addressed. Due to the differences in the results obtained by different mutation testing methods, the M-K mutation test in this study was only used to preliminarily obtain the year of possible mutation, and a more systematic mutation analysis needs further study. In addition, there are differences between seasonal and monthly temperature extremes, and the selection of indices can be further improved. This study failed to make a quantitative assessment and analysis of the disaster risk results of each extreme temperature index. In the future, based on the analysis of the spatial and temporal characteristics of extreme temperature and the results of future change prediction, combined with social, economic, and environmental indicators of the basin, a comprehensive risk evaluation of meteorological disasters should be studied.

6. Conclusion

To explore the simulation and early warning assessment of extreme temperatures, quantitatively evaluate and describe extreme events, and reduce the adverse effects of frequent extreme events on the ecological environment, social economy, and human production, the temporal-spatial characteristics and future change trends of extreme temperature were studied in the Longtan watershed. It is expected to provide a reference for the establishment of extreme climate event early warning systems, the formulation of disaster prevention and mitigation plans, and the operation and management of water conservancy projects. It was found that (1) from 1959 to 2017, the extreme temperature in the Longtan watershed changed significantly and showed a warming trend. The extreme temperature indices with significant trends all showed abrupt changes, mainly occurring in the 1980s, 1990s, and after 2000. (2) The spatial distribution of extreme temperature indices is generally increasing or decreasing from southwest to northeast, with alternating positive and negative phases over time and obvious fluctuations. Most of the indices have the following spatial variation characteristics: ① spatial variation consistency; ② southwest more northeast less or southwest less northeast more distribution. (3) The analysis of the future trend of extreme temperature indices from 2021 to 2050 using the GF3 model at Luxi station and NE1 model at Xingren station found that the high-temperature area above 33.7°C increased with the increase of emission concentration. The temperature in the basin shows a warming trend, and the risk of extreme high temperatures may exist in the downstream area in the future. In response to the warming trend of extreme temperature, it is recommended that the management in the watershed should pay more attention to extreme temperature events and take measures such as establishing safe public drinking water areas to reduce the hazards of extreme heat events. In addition, this study failed to quantitatively analyze the disaster risk results of each extreme temperature index, and future studies should be based on this study to combine various socioeconomic indicators to conduct a comprehensive risk evaluation of extreme temperature disasters.

Data Availability

The historical observations of daily maximum and daily minimum temperatures were obtained from the China Meteorological Data Center (https://data.cma.cn/wa). The data of the climate models were obtained from the CMIP5 official website (https://esgf-node.llnl.gov/search/cmip5/).

Conflicts of Interest

The authors declare that there are no conflicts of interest regarding the publication of this paper.

Acknowledgments

The research was supported by the National Natural Science Foundation of China (51969004 and 51979038), the Guangxi Natural Science Foundation of China (2017GXNSFAA198361), and the Innovation Project of Guangxi Graduate Education (YCBZ2019022).

References

[1] I. Lun, M. Ohba, and S. Morikami, "An overview of extreme hot weather incidents and the role of natural ventilation in buildings on human body comfort," *International Journal of Ventilation*, vol. 11, no. 3, pp. 311–322, 2012.

[2] J. Yamaguchi, Y. Kanno, G. Chen, and T. Iwasaki, "Cold air mass analysis of the record-breaking cold surge event over east Asia in january 2016," *Journal of the Meteorological Society of Japan*, vol. 97, no. 1, pp. 275–293, 2019.

[3] X. Shen, B. Liu, G. Li et al., "Spatiotemporal change of diurnal temperature range and its relationship with sunshine duration and precipitation in China," *Journal of Geophysical Research: Atmospheres*, vol. 119, no. 23, pp. 13163–13179, 2014.

[4] X. Shen, B. Liu, X. Lu, and G. Fan, "Spatial and temporal changes in daily temperature extremes in China during 1960–2011," *Theoretical and Applied Climatology*, vol. 130, pp. 933–943, 2017.

[5] X. Shen, B. Liu, and X. Lu, "Weak cooling of cold extremes versus continued warming of hot extremes in China during the recent global surface warming hiatus," *Journal of Geophysical Research: Atmospheres*, vol. 123, no. 8, pp. 4073–4087, 2018.

[6] M. Iturbide, A. Casanueva, J. Bedia, S. Herrera, J. Milovac, and J. M. Gutierrez, "On the need of bias adjustment for more plausible climate change projections of extreme heat," *Atmospheric Science Letters*, vol. 23, no. 2, 2022.

[7] K. L. Ebi, J. Vanos, J. W. Baldwin et al., "Extreme weather and climate change: population health and health system implications," *Annual Review of Public Health*, vol. 42, no. 1, pp. 293–315, 2021.

[8] L. V. Alexander, "Global observed long-term changes in temperature and precipitation extremes: a review of progress and limitations in IPCC assessments and beyond," *Weather and Climate Extremes*, vol. 11, pp. 4–16, 2016.

[9] Y. F. Xiong, Z. J. Ta, M. Gan et al., "Evaluation of CMIP5 climate models using historical surface air temperatures in central Asia," *Atmosphere*, vol. 12, no. 3, p. 308, 2021.

[10] J. H. Stillman, "Heat waves, the New normal: summertime temperature extremes will impact animals, ecosystems, and human communities," *Physiology*, vol. 34, no. 2, pp. 86–100, 2019.

[11] S. A. Changnon, R. A. Pielke, D. Changnon, R. T. Sylves, and R. Pulwarty, "Human factors explain the increased losses from weather and climate extremes," *Bulletin of the American Meteorological Society*, vol. 81, no. 3, pp. 437–442, 2000.

[12] F. T., L. J. Supari, E. Aldrian, and L. Juneng, "Observed changes in extreme temperature and precipitation over Indonesia," *International Journal of Climatology*, vol. 37, no. 4, pp. 1979–1997, 2017.

[13] T. Caloiero, "Trend of monthly temperature and daily extreme temperature during 1951–2012 in New Zealand," *Theoretical and Applied Climatology*, vol. 129, pp. 111–127, 2017.

[14] A. Poudel, L. Cuo, J. Ding, and A. R. Gyawali, "Spatio-temporal variability of the annual and monthly extreme temperature indices in Nepal," *International Journal of Climatology*, vol. 40, no. 11, pp. 4956–4977, 2020.

[15] S. Mohan, R. M. Clarke, and X. T. Chadee, "Variations in extreme temperature and precipitation for a Caribbean island: Barbados (1969–2017)," *Theoretical and Applied Climatology*, vol. 140, pp. 1277–1290, 2020.

[16] J. H. Yang, Z. Jiang, and Z. H. Jiang, "Characteristics of extreme temperature event and its response to regional warming in Northwest China in past 45 years," in *Proceedings of the 2008 2nd International Conference on Bioinformatics and Biomedical Engineering*, no. 1, pp. 70–76, Shanghai, China, May 2008.

[17] X. W. Liu and Z. X. Xu, "Spatial and temporal pattern of extreme temperature during 1961–2018 in China," *Journal of Water and Climate Change*, vol. 11, no. 4, pp. 1633–1644, 2020.

[18] W. Zhan, X. G. He, J. Sheffield, and E. F. Wood, "Projected seasonal changes in large-scale global precipitation and temperature extremes based on the CMIP5 ensemble," *Journal of Climate*, vol. 33, no. 13, pp. 5651–5671, 2020.

[19] C. K. Folland, C. Miller, D. Bader et al., "Workshop on indices and indicators for climate extremes, Asheville, NC, USA, 3–6 June 1997 - breakout group C: temperature indices for climate extremes," *Weather and Climate Extremes*, vol. 42, no. 1, pp. 31–43, 1999.

[20] X. C. Chen, Y. Xu, C. H. Xu, and Y. Yao, "Assessment of precipitation simulations in China by CMIP5 multi-models," *Progressus Inquisitiones de Mutatione Climatis*, vol. 10, no. 3, pp. 217–225, 2014.

[21] H. Xiao, G. H. Lu, Z. Y. Wu, and Z. Liu, "Flood response to climate change in the pearl river basin for the next three decades," *Journal of Hydraulic Engineering*, vol. 44, no. 12, pp. 1409–1419, 2013.

[22] M. S. Jahangir and S. Moghim, "Assessment of the urban heat island in the city of Tehran using reliability methods," *Atmospheric Research*, vol. 225, pp. 144–156, 2019.

[23] V. Gumus, "Spatio-temporal precipitation and temperature trend analysis of the seyhan-ceyhan river basins, Turkey," *Meteorological Applications*, vol. 26, no. 3, pp. 369–384, 2019.

[24] I. K. Tsanis and A. H. El-Shaarawi, "Trend evaluation of water quality parameters in the Niagara and St. Lawrence Rivers," *Environmental Monitoring and Assessment*, vol. 23, no. 1, pp. 205–218, 1992.

[25] P. Mahmoudi, M. Mohammadi, and H. Daneshmand, "Investigating the trend of average changes of annual temperatures in Iran," *International Journal of Environmental Science and Technology*, vol. 16, no. 2, pp. 1079–1092, 2019.

[26] R. S. Du, F. H. Shang, and N. Ma, "Automatic mutation feature identification from well logging curves based on sliding *t* test algorithm," *Cluster Computing*, vol. 22, no. S6, pp. 14193–14200, 2019.

[27] M. G. Kendall, *Rank Correlation Methods*, Hafner Publishing Co, Oxford, UK, 2nd edition, 1955.

[28] H. B. Mann, "Nonparametric tests against trend," *Econometrica*, vol. 13, no. 3, pp. 245–259, 1945.

[29] L. A. Vincent and E. Mekis, "Changes in daily and extreme temperature and precipitation indices for Canada over the twentieth century," *Atmosphere-Ocean*, vol. 44, no. 2, pp. 177–193, 2006.

[30] A. Teshome and J. Zhang, "Increase of extreme drought over Ethiopia under climate warming," *Advances in Meteorology*, vol. 2019, Article ID 5235429, 18 pages, 2019.

[31] K. C. Schuenemann and J. J. Cassano, "Changes in synoptic weather patterns and Greenland precipitation in the 20th and 21st centuries: 1. Evaluation of late 20th century simulations from IPCC models," *Journal of Geophysical Research*, vol. 114, Article ID D20113, 2009.

[32] J. Sillmann, V. V. Kharin, F. W. Zwiers, X. Zhang, and D. Bronaugh, "Climate extremes indices in the CMIP5 multimodel ensemble: Part 2. Future climate projections," *Journal of Geophysical Research: Atmospheres*, vol. 118, no. 6, pp. 2473–2493, 2013.

[33] H. Zheng, F. H. S. Chiew, S. Charles, and G. Podger, "Future climate and runoff projections across South Asia from CMIP5 global climate models and hydrological modelling," *Journal of Hydrology: Regional Studies*, vol. 18, pp. 92–109, 2018.

[34] R. Rajbhandari, A. B. Shrestha, S. Nepal, and S. Wahid, "Projection of future climate over the koshi River basin based on CMIP5 GCMs," *Atmospheric and Climate Sciences*, vol. 06, no. 02, pp. 190–204, 2016.

[35] C. F. McSweeney, R. G. Jones, R. W. Lee, and D. P. Rowell, "Selecting CMIP5 GCMs for downscaling over multiple regions," *Climate Dynamics*, vol. 44, pp. 3237–3260, 2015.

[36] T. M. Leong, J. Liew, T. F. Tangang, C. J. Xiang, and R. B. Radin Firdaus, "Changes in temperature extremes and their relationship with ENSO in Malaysia from 1985 to 2018," *International Journal of Climatology*, vol. 41, 2020.

[37] J. Lee, "Future trend in seasonal lengths and extreme temperature distributions over South Korea," *Asia-Pacific Journal of Atmospheric Sciences*, vol. 53, no. 1, pp. 31–41, 2017.

[38] L. V. Alexander, X. Zhang, T. C. Peterson et al., "Global observed changes in daily climate extremes of temperature and precipitation," *Journal of Geophysical Research: Atmospheres*, vol. 111, p. 22, 2006.

[39] X. Y. Wang, Y. Q. Li, M. M. Wang et al., "Changes in daily extreme temperature and precipitation events in mainland China from 1960 to 2016 under global warming," *International Journal of Climatology*, vol. 41, no. 2, pp. 1465–1483, 2020.

[40] Y. Jia, "Study on the temporal and spatial distribution of extreme temperature in Liaoning province based on EOF analysis," *Journal of Anhui Agricultural Sciences*, vol. 36, no. 11, pp. 4589-4590, 2008.

[41] Y. Guo, J. Tan, B. Y. Cheng, and D. L. Ma, "A kinetic model structure for delayed fluorescence from plants," *Biosystems*, vol. 95, no. 2, pp. 98–103, 2009.

[42] W. Wu, H. Z. Mu, Z. R. Liang, and X. C. Liu, "Projected changes in extreme temperature and precipitation events in Shanghai based on CMIP5 simulations," *Climatic and Environmental Research*, vol. 21, no. 3, pp. 269–281, 2016.

[43] W. W. Xiao, B. Wang, D. L. Liu, and P. Feng, "Projecting changes in temperature extremes in the Han River Basin of China using downscaled CMIP5 multi-model ensembles," *Atmosphere*, vol. 11, no. 4, p. 424, 2020.

[44] M. M. Li, M. G. Zhou, J. Yang, P. Yin, B. Wang, and Q. Liu, "Temperature, temperature extremes, and cause-specific respiratory mortality in China: a multi-city time series analysis," *Air Quality, Atmosphere & Health*, vol. 12, no. 5, pp. 539–548, 2019.

[45] M. G. Haile, T. Wossen, K. Tesfaye, and J. von Braun, "Impact of climate change, weather extremes, and price risk on global food supply," *Economics of Disasters and Climate Change*, vol. 1, no. 1, pp. 55–75, 2017.

[46] J. Wang, Z. W. Yan, Z. Li, W. D. Liu, and Y. Wang, "Impact of urbanization on changes in temperature extremes in Beijing during 1978–2008," *Chinese Science Bulletin*, vol. 58, no. 36, pp. 4679–4686, 2013.